Chlorophyll Production in the Amundsen Sea Boosts Heat Flux to Atmosphere and Weakens Heat Flux to Ice Shelves

A. G. Twelves[1,2] , D. N. Goldberg[2] , P. R. Holland[3] , S. F. Henley[2] , M. R. Mazloff[4] , and D. C. Jones[3,5]

[1]Finnish Meteorological Institute, Helsinki, Finland, [2]School of GeoSciences, University of Edinburgh, Edinburgh, UK, [3]British Antarctic Survey, NERC, UKRI, Cambridge, UK, [4]Scripps Institution of Oceanography, University of California San Diego, La Jolla, CA, USA, [5]Cooperative Institute for Great Lakes Research, University of Michigan, Ann Arbor, MI, USA

Abstract The Amundsen Sea in West Antarctica features rapidly thinning ice shelves, large polynyas, and sizable spring phytoplankton blooms. Although considerable effort has gone into characterizing heat fluxes between the Amundsen Sea, its associated ice shelves, and the overlying atmosphere, the effect of the phytoplankton blooms on the distribution of heat remains poorly understood. In this modeling study, we implement a feedback from biogeochemistry onto physics into MITgcm-BLING and use it to show that high levels of chlorophyll—concentrated in the Amundsen Sea Polynya and the Pine Island Polynya—have the potential to increase springtime surface warming in polynyas by steepening the attenuation profile of solar radiation with depth. The chlorophyll-associated warm anomaly (on average between +0.2°C and +0.3°C) at the surface is quickly dissipated to the atmosphere, by increases in longwave, latent and sensible heat loss from open water areas. Outside of the coastal polynyas, the summertime warm anomaly leads to an average sea ice thinning of 1.7 cm across the region, and stimulates up to 20% additional seasonal melting near the fronts of ice shelves. The accompanying cold anomaly, caused by shading of deeper waters, persists year-round and affects a decrease in the volume of Circumpolar Deep Water on the continental shelf. This cooling ultimately leads to an average sea ice thickening of 3.5 cm and, together with associated changes to circulation, reduces basal melting of Amundsen Sea ice shelves by approximately 7% relative to the model scenario with no phytoplankton bloom.

Plain Language Summary Near the Antarctic coastline the sea ice cover is broken by patches of open water, called polynyas, which often undergo a visible change in color from blue to green as spring progresses. This is due to the chlorophyll produced in blooms of microscopic algae. Here we use computer simulations to investigate the impact of this change in color on the delicate system of ice and ocean in the Amundsen Sea region of west Antarctica. We find that the "greening" of polynyas helps to trap more of the sun's energy close to the sea surface, but that this excess heat is then released back to the atmosphere over the course of the summer. Meanwhile, the deeper waters of the polynya are exposed to less energy from the sun and therefore are cooler than they would be if there were no algae bloom. Ultimately, the cooling of deep waters across the Amundsen Sea weakens the transport of heat toward the continent. Our computer simulations show that, as a result, ice shelves melt around 7% slower when large algae blooms are present compared to when the surface waters are clear.

1. Introduction

The west Antarctic coastline is characterized by annually recurring areas of open water—polynyas—within the sea ice pack. In the Amundsen Sea there are two such coastal polynyas, both of which host large spring phytoplankton blooms (Arrigo & Van Dijken, 2003; Arrigo et al., 2012; Park et al., 2017). The Amundsen Sea Polynya (ASP) forms downwind of a line of icebergs grounded on Bear Ridge, and is bounded to the south by the front of Dotson Ice Shelf (DIS). The Pine Island Polynya (PIP) forms within Pine Island Bay and abuts the fronts of the Cosgrove and Thwaites Glacier Ice Shelves (TGIS) as well as the Pine Island Glacier Ice Shelf (PIGIS). Each of these ice shelves shows signs of thinning and/or grounding line retreat in satellite observations (Christie et al., 2016; Gourmelen et al., 2017; Shean et al., 2019; Shepherd et al., 2019), whilst the two polynyas exhibit exceptionally high primary productivity (Alderkamp et al., 2012; Arrigo & Van Dijken, 2003; Arrigo et al., 2015). In this modeling study we investigate the effect of the spring phytoplankton bloom on heat fluxes from polynyas to the atmosphere and from the ocean to ice shelf fronts.

The deepest waters in the Amundsen Sea consist of Circumpolar Deep Water (CDW), originating in the Antarctic Circumpolar Current. This water mass arrives at the Amundsen Sea via a small number of troughs at the continental shelf break. Mixing of CDW on the shelf produces a modified Circumpolar Deep Water (mCDW) mass, which ultimately flows into ice shelf cavities and stimulates basal melting (Arneborg et al., 2012; Jacobs et al., 1992). Rising buoyant meltwater in turn generates an overturning circulation—the meltwater pump— within ice shelf cavities, which pulls dissolved iron from depth to the surface (Dinniman et al., 2020; Oliver et al., 2019; Twelves et al., 2020). Above the warm and saline mCDW layer there is a cold and slightly less saline Winter Water (WW) layer, and above that a seasonally warmed layer of fresh Antarctic Surface Water (AASW).

Ocean stratification within the ASP and PIP is sensitive to summertime insolation and to inputs of ice shelf and sea ice meltwater, which all tend to stabilize the water column, and to winds, which tend to destabilize the water column. The latter effect occurs both directly through wind stress and indirectly by driving a net export of freshwater in wind-blown sea ice (Bett et al., 2020; Zheng et al., 2021). This stratification in turn impacts phytoplankton growth, with springtime stability helping to alleviate light limitation, before mixing in autumn and winter resupplies nutrients—most crucially iron—from depth before the next growth season (St-Laurent et al., 2017). Whilst wind-driven vertical mixing is a dominant source of iron to other Antarctic seas, in the Amundsen Sea it plays a secondary role compared to the iron associated with ice shelf melting (Dinniman et al., 2020; Oliver et al., 2019; Twelves et al., 2020).

Numerous studies have investigated the role of Amundsen Sea ice shelves in stimulating phytoplankton growth– using in situ measurements (Gerringa et al., 2012; Yager et al., 2016), satellite data (Arrigo & Van Dijken, 2003; Park et al., 2017), and biogeochemical modeling (Oliver et al., 2019; St-Laurent et al., 2019; Twelves et al., 2020). Less attention has been paid to the effect that very high summer chlorophyll concentrations–locally up to 10 mg m^{-3}—have on the attenuation of shortwave radiation, and thus on the heat available to drive basal melting.

The important contribution of chlorophyll to ocean heat fluxes was initially demonstrated in coarse global models of the ocean (Manizza et al., 2005). Subsequent studies have included this "bio-optical feedback" in regional models and with a focus on different aspects of the heat budget. Implementation in tropical regions (Hernandez et al., 2017) showed a cooling of waters upwelling from depth, whilst other studies, extended to include the effects of colored dissolved organic matter (CDOM), have shown reduced Arctic sea ice cover (Pefanis et al., 2020) and increased heat fluxes to the atmosphere from the Baltic Sea (Cahill et al., 2023). This feedback remains important in coupled ocean-atmosphere models, with phytoplankton blooms shown to impact storm tracks (Gnanadesikan et al., 2010) and marine heatwaves (Gnanadesikan et al., 2019).

However, until now, this feedback from biology onto physics has been disregarded in models of the Amundsen Sea and, to our knowledge, in ice shelf modeling more generally. Instead, even state-of-the-art models represent shortwave attenuation using spatially homogeneous and time-invariant extinction coefficients. Commonly the surface waters are assumed to absorb light to a similar degree as surface waters in oligotrophic regions, even where observations and/or biogeochemical models show intense chlorophyll production close to ice shelves during the spring and summer. As a result, shortwave radiation toward the base of the mixed layer is systematically overestimated, and these ice-ocean models include an artificial source of heat in this part of the water column.

One solution to this problem is to include the attenuation coefficient as an additional free parameter when tuning ice-ocean models to accurately reproduce basal melt rates. However it is already well established that the attenuation of light correlates strongly with chlorophyll in the Southern Ocean (Dutkiewicz et al., 2015), and moreover that attenuation shows strong seasonal variation as a result. The use of a time-invariant attenuation profile would thus be unsuitable, whilst the tuning of multiple profiles—for different seasons—would add substantial complexity to the model development process.

Another approach is to use surface chlorophyll data—derived from satellite measurements of ocean color—as an additional input to the model. However, since satellite imagery only captures the ocean surface, this requires an additional step in extrapolating surface attenuation over the entire euphotic zone, and analysis has shown that chlorophyll estimates from satellite measurements can be unreliable in Antarctic coastal polynyas (Dierssen & Smith, 2000). Furthermore, using chlorophyll data to drive the model introduces a potential mismatch between the chlorophyll concentration used as forcing for the model and those aspects of the model dynamics (sea ice retreat, changes to stratification) that would influence phytoplankton growth.

In this study we seek instead to quantify the net contribution of chlorophyll to the ice-ocean system via a two-way coupling of MITgcm to the Biology Light Iron Nutrients and Gases (BLING) model. Chlorophyll output from the biogeochemical model is used at every time step to calculate the vertical distribution of shortwave heating in the physical model. Whilst entailing a higher computational cost, this approach captures the seasonality of the euphotic depth and ensures that it is consistent with the seasonality of the hydrodynamic model. Furthermore, this strategy allows us to make a quantitative estimate for the impact of a biological process—the iron- and light-limited growth of phytoplankton—on the heat fluxes between atmosphere, sea ice, and ice shelves in the Amundsen Sea.

2. Methods

2.1. Modeling Rationale

We integrate the Manizza et al. (2005) formulation for attenuation by chlorophyll into the thermodynamics of MITgcm, using the BLING model to simulate biogeochemical processes (Galbraith et al., 2010). We apply this two-way coupled model to a domain covering the entire Amundsen Sea, and focus our attention on air-sea heat fluxes, sea ice and basal melting on the continental shelf. We choose to compare a model run with chlorophyll generated by BLING to a model run without chlorophyll, emphasizing two key points:

- Existing models of the Amundsen Sea (and other parts of the Antarctic continental shelf) contain an implicit contribution of chlorophyll (generally a substantial underestimate) in the form of water type (Jerlov, 1976). Thus the changes we observe are not equivalent to the error in existing model setups, which have themselves been tuned using a water-type setup from the start (Assmann et al., 2013; St-Laurent et al., 2015). Instead they represent the sensitivity of the model, as tuned, to the addition or removal of chlorophyll.
- In the real world, entirely chlorophyll-free summertime conditions do not and will not occur in the Amundsen Sea. Thus our results do not represent forecasts but should instead be understood as quantifying the contribution of chlorophyll to ice-ocean heat fluxes, and as a demonstration of a hitherto neglected two-way coupling between ice shelves and phytoplankton blooms.

Our approach—quantifying the contribution of a water constituent to attenuation using a zero case as control—is similar to that taken by Gnanadesikan et al. (2019) in quantifying the impact of CDOM on extreme sea surface temperatures.

2.2. Physical Model

We simulate ice-ocean interactions with the Massachusetts Institute of Technology general circulation model (MITgcm checkpoint 67c; Marshall et al., 1997), including the packages for sea ice (Losch et al., 2010) and for static ice shelves (Losch, 2008). Vertical mixing—an important control on biogeochemical processes—is represented using the K-profile parameterization (KPP) developed by Large et al. (1994).

Our domain contains several ice shelves, from Getz Ice Shelf in the west to Abbott Ice Shelf in the east (Figure 1), and stretches north beyond the continental shelf break. Horizontal resolution decreases from 2.8 km at the coastline to 5.2 km at the northern boundary, whilst vertical resolution decreases from 10 m at the surface to 200 m in the deepest layer. Both our bathymetry and our ice shelf topography are based on BedMachine Version 1 (Morlighem et al., 2020). However, as in St-Laurent et al. (2017) and Bett et al. (2020), we also include a grounded iceberg "wall" northwards of Bear Island, which blocks westward advection of sea ice. This feature has been shown to be important both for accurate representation of the physical system (Bett et al., 2020) and for simulating the spring phytoplankton bloom in the ASP (Twelves et al., 2020). In addition, we prescribe a freshwater flux over the upper 300 m close to the coastline, intended to represent drifting icebergs.

We source boundary conditions for temperature and salinity from the World Ocean Atlas climatology (Locarnini et al., 2018; Zweng et al., 2019), and for velocities from the B-SOSE state estimate (Verdy & Mazloff, 2017). B-SOSE also provides us with boundary conditions for sea ice (concentration, thickness, velocity, and snow depth). We derive our atmospheric forcing from the ERA5 reanalysis (1979–2018; (Hersbach et al., 2020)).

This domain was first described in Assmann et al. (2013), where it was used to simulate conditions in the Amundsen Sea since the first oceanographic observations were conducted there in 1994. It was then further
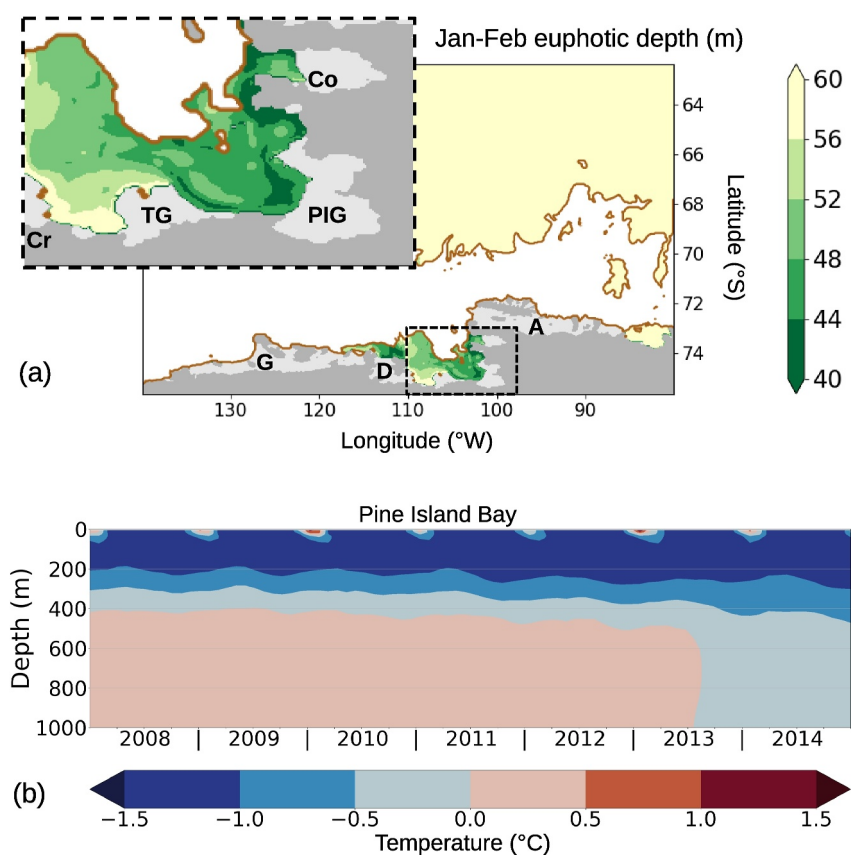
Figure 1. (a) The model domain covers the entire Amundsen Sea and includes two major polynyas plus the seven ice shelves labeled: Abbot (A), Dotson (D), Getz (G), Crosson (Cr), Thwaites Glacier (TG), Cosgrove (Co) and pine island glacier. The inset is a closeup view of the area enclosed by the dashed line, covering Pine Island Bay. The boundary of the continental shelf approximately follows a 1,000 m isobath. The colormap shows the modeled springtime euphotic depth in open-water areas, averaged over January and February across the entire model run. The sea ice coverage (concentration >15%) is shown in white. (b) Evolution of the vertical structure in temperature within the Pine Island Bay sub-domain, showing the onset of convection during 2013.

developed and validated in Kimura et al. (2017) and Bett et al. (2020). Using outputs from an ensemble of earth system models as forcing, Naughten et al. (2022) were able to apply the same model setup to investigate changes in the Amundsen Sea since the early twentieth century. Naughten et al. (2022) reported a reduction in instances of convective cooling on the continental shelf over this period. However the model also has a tendency to undergo periods of convection close to ice shelf fronts in recent years, conflicting with observations.

For the remainder of this study we treat those "convection periods", which disagree with contemporary observations (but that may be representative of past Amundsen Sea conditions) separately from the rest of the study period. Such convection may be viewed as loosely representative of conditions at those locations around Antarctica where convection is currently observed. We discard the 2-year convection period that we identify in our results from our core analysis and from our calculation of time-averaged anomalies due to chlorophyll. Nonetheless we still share these results, as a means of widening the scope of our study beyond the Amundsen Sea continental shelf.

Our setup is closest to that used by Goldberg et al. (2023), who describe several key differences with the setup used by Naughten et al. (2022). In the present study we introduce phytoplankton blooms to the model, via a modified coupling of MITgcm to the BLING model (Galbraith et al., 2010).

2.3. Biogeochemical Model

Previous work has shown that BLING is able to reproduce iron-light colimited phytoplankton blooms, both in the Amundsen Sea (Twelves et al., 2020) and elsewhere (Castro de la Guardia et al., 2019; Galbraith et al., 2010). In this study, as in Twelves et al. (2020), we employ an additional tracer for advected biomass in addition to the eight core tracers (dissolved inorganic carbon (DIC), total alkalinity, oxygen, nitrate, phosphate, iron, dissolved organic nitrogen (DON) and dissolved organic phosphorus (DOP)). Again following Twelves et al. (2020), as well as St-Laurent et al. (2019), we prescribe a concentration of 20 μmol m^{-3} for iron dissolved in glacial meltwater. The remaining biogeochemical tracers are neither sourced from nor diluted by glacial meltwater in our setup. Similarly we do not include the effects of sea ice or atmospheric deposition on tracer concentrations.

Starting from a monthly climatology of BSOSE (2008–2012 solution, Verdy & Mazloff (2017)), we generate lateral boundary conditions for each of the eight core tracers. The tracers are nudged toward the boundary conditions using the MITgcm RBCS package with a timescale of 1 day. For the additional tracer representing advected biomass we instead relax the tracer to zero at the boundaries. Incoming photosynthetically available radiation (PAR) is calculated within the model as 40% of the total incoming shortwave radiation (from the ERA5 reanalysis).

After first spinning up the physical model from 1 January 1979 (with an initial condition itself seeded from a preliminary 24 years run), we deploy passive tracers from 1 January 1995. From 1 January 2003 we enable BLING and at the same time switch the shortwave attenuation scheme from one based on Jerlov water type (Jerlov, 1976) to one which treats water molecules and chlorophyll separately. We spin up each of the following experiments for a further 5 years, before analyzing the outputs from 1 January 2008 to 31 December 2014.

For the *GREEN* experiment we include large and small classes of phytoplankton, which are treated separately in BLING but whose aggregate forms the biomass tracer advected around the domain (Twelves et al., 2020; Verdy & Mazloff, 2017). The large class represent diatoms, whilst the small class represents *Phaeocystis antarctica*; together these have been observed to constitute the large majority of biomass in the Amundsen Sea (Lee et al., 2022). We account for the higher iron requirement of *P. antarctica* compared to diatoms by allocating the former a half saturation constant of 0.2μmol m^{-3} and the latter a half saturation constant of 0.15μmol m^{-3} (following Nissen & Vogt (2021)).

For the *BLUE* experiment we artificially set the growth rate to zero for both phytoplankton classes, leaving only a very small detrital biomass to be advected around the domain. This detritus is several orders of magnitude smaller than the biomass in *GREEN*, so we can consider *BLUE* to represent chlorophyll-free conditions in the Amunsdsen Sea. The difference in outputs *GREEN − BLUE* thus provides us with a proxy with which to quantify the impact of chlorophyll on shortwave heating and on the ice-ocean system as a whole.

2.4. Shortwave Heating

In the Jerlov water type formulation (Jerlov, 1976), used by default in MITgcm and also in the spin up of our model prior to 2003, attenuation of light is homogeneous in both time and space. Each water type corresponds to a single attenuation profile representing a different mixture of optically active constituents, without explicitly resolving any one of those constituents.

The Jerlov water type approach is characterized by simplicity. Just three numbers are required to uniquely specify each type: an attenuation constant for visible light, an attenuation coefficient for near-infrared light, and the ratio of the two components in the incoming power spectrum. Previous modeling of the Amundsen Sea (Goldberg et al., 2023; Kimura et al., 2017; Naughten et al., 2022) using MITgcm assumed Jerlov water type IA, with visible light extinction of 0.05 m^{-1} representing relatively clear waters.

However, as argued above, the use of Jerlov water type is in fact unsuitable for the Amundsen Sea. In this study we instead use the Manizza et al. (2005) formulae for shortwave attenuation in the physical model. These are the same equations previously implemented in BLING to calculate PAR for phytoplankton by Twelves et al. (2020). Our approach here diverges from the Jerlov water-type approach in two ways. Firstly, the visible part of the spectrum I_{vis} (measured in W m^{-2}) is divided into two components, I_{red} and I_{bg}, representing the red and blue-green components respectively:

$$I_{vis} = I_{red} + I_{bg}. \tag{1}$$

These two components have equal power at the surface but are attenuated at different rates with respect to depth z in the water column:

$$\frac{\partial I_{red}}{\partial z} = -\kappa_{red}(z) I_{red}(z), \tag{2}$$

$$\frac{\partial I_{bg}}{\partial z} = -\kappa_{bg}(z) I_{bg}(z). \tag{3}$$

Secondly, and more importantly for our study, the attenuation coefficients (κ_{red} and κ_{bg}, measured in units of m^{-1}) for the two light bands are expressed as sums of contributions from water molecules and from the chlorophyll concentrations calculated in BLING:

$$\kappa_{red} = \kappa_{red}^0 + \chi_{red}[Chl]^{e_{red}}; \tag{4}$$

$$\kappa_{bg} = \kappa_{bg}^0 + \chi_{bg}[Chl]^{e_{bg}}. \tag{5}$$

Here κ_{red}^0 and κ_{bg}^0 (measured in m^{-1}), χ_{red} (units of mg$^{-e_{red}}$ m^{-1}), χ_{bg} (units of mg$^{-e_{bg}}$ m^{-1}), e_{red} and e_{bg} are constants as in Twelves et al. (2020). Attenuation by other optically active constituents of seawater, such as CDOM or detritus, is not resolved in BLING and thus is excluded from this study.

By extending this light attenuation scheme from BLING (where it affects the PAR available to phytoplankton (Twelves et al., 2020),) to the physical model, we achieve consistency between the physical and biogeochemical models, and allow the latter to feed back onto the former. The attenuation of shortwave radiation contributes to the heat budget in MITgcm, and thus the distribution of phytoplankton growth affects the vertical distribution of heat.

Chlorophyll can also directly affect the albedo at the sea surface (Yu et al., 2022). However in our modeling study we keep ocean albedo constant, so that the only direct impact of chlorophyll on physics is via the attenuation of radiation in the ocean interior. This in turn changes the distribution of heat, which alters the sea ice distribution and air-sea heat fluxes.

2.5. Calculation of Euphotic Depth

We gather in situ observations of euphotic depth from the study of Park et al. (2017), which used an underwater irradiance sensor, and satellite-derived estimates from the GlobColour database (http://hermes.acri.fr). To verify the applicability of the optical model to the Amundsen Sea, we use the in situ observations of surface chlorophyll from Park et al. (2017) and calculate the euphotic depth which these would predict using the Manizza et al. (2005) formulation. Using the Manizza et al. (2005) formulae, the euphotic depth Z_{eu} is defined by the equation

$$I_0 \frac{e^{-\kappa_{red} Z_{eu}} + e^{-\kappa_{bg} Z_{eu}}}{2} = \frac{I_0}{100}, \tag{6}$$

where I_0 is the surface irradiance. A comparison against the PAR sensor-derived euphotic depth shows good agreement for most stations (Figure S1 in Supporting Information S1), despite the fact that the Manizza et al. (2005) coefficients were originally derived from a global data set (Morel, 1988).

In MITgcm we implement the euphotic depth as a diagnostic by first calculating the ratio of in situ and surface irradiance—based on model chlorophyll concentrations—at every cell center and cell face. The euphotic depth is calculated by linear interpolation between the deepest center (face) point where $I > \frac{I_0}{100}$ and the shallowest face (center) point where $I < \frac{I_0}{100}$. The fit between modeled and observed euphotic depth is thus a product of both the bio-optical model skill and the biogeochemical model skill.

2.6. Surface Heat Fluxes

The air-sea heat balance in MITgcm comprises both radiative (i.e., shortwave, longwave) and turbulent (i.e., sensible, latent) heat fluxes.

The shortwave heat flux per unit area at the surface F_{SW} is sensitive only to the external forcing SW_{down} and to the sea ice coverage. In ice-free seas, the incoming shortwave is modified only by the water albedo α_{ocean}, which is fixed (at a value of 0.1) in our model setup:

$$F_{SW} = (1 - \alpha_{ocean}) SW_{down}. \tag{7}$$

The distribution of this heating over the water column then depends on the attenuation profile, which in turn is determined by chlorophyll concentration as described above.

In contrast the longwave heat flux per unit area F_{LW} comprises not only the incoming forcing LW_{down} but also the outgoing flux. The latter is calculated via a Stefan-Boltzmann law depending on the sea surface temperature T_{SURF},

$$F_{LW} = LW_{down} - \sigma T_{SURF}^4, \tag{8}$$

where σ is the Stefan-Boltzmann constant.

The sensible heat flux per unit area in MITgcm is calculated as

$$F_{SEN} = \rho_{atm} c_{p_{atm}} u_s c_u c_T \Delta T \tag{9}$$

where ρ_{atm} is the atmospheric density, u_s is the wind speed and ΔT is the difference between sea surface and atmospheric temperatures. The calculation of the bulk exchange coefficients c_u and c_T follows Bryan et al. (1996), and $c_{p_{atm}}$ is equal to the specific heat capacity at atmospheric pressure.

Similarly the latent heat flux per unit area is given by

$$F_{LAT} = \rho_{atm} L u_s c_u c_q \Delta q \tag{10}$$

where L is the latent heat of vaporzation, Δq is the difference between atmospheric humidity and the saturated humidity, and c_q is an additional bulk exchange coefficient (Bryan et al., 1996). These coefficients and fluxes are solved iteratively at each time step within MITgcm.

On the Amundsen Sea continental shelf, the total area-integrated heat flux at the ocean surface $\mathbb{F}_{SURF}$ can be separated into a component $\mathbb{F}_{SICE}$ representing ice-covered sea surface, and a component $\mathbb{F}_{OPEN}$ representing ice-free–polynya–model sea surface.

$$\mathbb{F}_{SURF} = \mathbb{F}_{SICE} + \mathbb{F}_{OPEN} \tag{11}$$

The term $\mathbb{F}_{SICE}$ includes contributions from the formation and melting of sea ice, as well as fluxes within leads between the ice floes. Accordingly, the MITgcm ocean heat calculations account both for the effect of sea ice cover in obstructing air-sea fluxes and for the additional fluxes into and out of the sea ice itself. A full analysis of the MITgcm surface heat budget in partially ice covered seas would require a detailed breakdown of the heat fluxes between air and sea ice. Since these are not provided as model diagnostics within the MITgcm, their calculation would demand changes to the model code that are beyond the scope of this study. Previous work with MITgcm on the components of the wider Southern Ocean heat budget discounted $\mathbb{F}_{SICE}$ by masking out a fixed region of the domain (Tamsitt et al., 2016), but this would be unsuitable at the scale of our study, where there is substantial interannual variability in the extent of coastal polynyas. Instead we use monthly outputs of the sea ice concentration, set a threshold of 10% coverage to distinguish $\mathbb{F}_{SICE}$ from $\mathbb{F}_{OPEN}$, and only calculate the components of the air-sea flux for the latter.
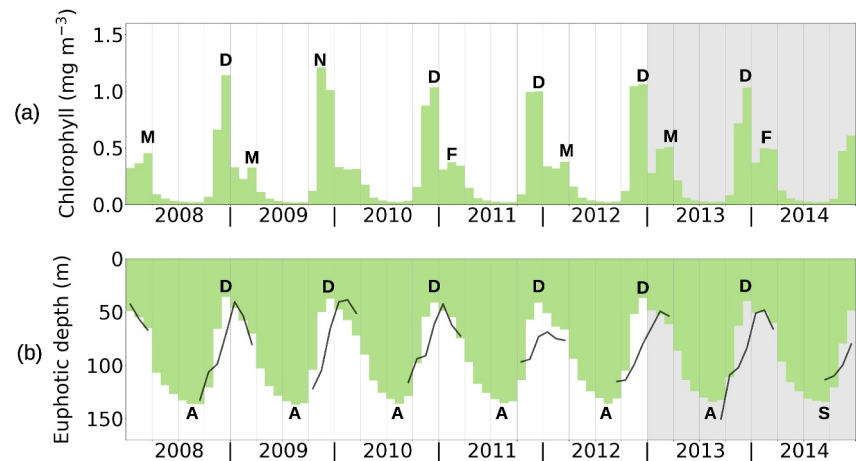
Figure 2. Quantities averaged over the Pine Island Bay region shown in Figure 1. The variation in chlorophyll in (a) is strongly seasonal, as is the euphotic depth plotted in (b). The month where the spring bloom peaks in (a) is marked for each year (N, November; D, December), as is the peak of the late summer bloom (where present, F, February; M, March). Similarly in (b) the minimum modeled euphotic depth timing is marked (D, December), and also the maximum euphotic depth (A, August; S, September) The black line in (b) shows the euphotic depth derived by GlobColour based on satellite observations. Gray shading marks the period of convection.

For an entirely ice-free portion of sea surface, $\mathbb{F}_{OPEN}$ is simply the sum of shortwave, longwave, sensible and latent heat fluxes:

$$\mathbb{F}_{OPEN} = \mathbb{F}_{SW} + \mathbb{F}_{LW} + \mathbb{F}_{SEN} + \mathbb{F}_{LAT} \tag{12}$$

where the blackboard bold font $\mathbb{F}$ is used to emphasize that the units are now integrated to W rather than Wm^{-2}, with all terms dependent on the extent of the open water area A.

3. Results

3.1. Chlorophyll and Light

Figure 1 shows that early summertime light attenuation (in *GREEN*) is substantially increased within both the ASP and the PIP (relative to other ice-free regions). The euphotic depth—defined here as the depth where the light level is 1% of that immediately below the sea surface—is greater than 60 m for most of the ice-free portion of the domain, both north of the ice cover and in Eltanin Bay to the east of Abbot Ice Shelf. In the totally chlorophyll-free waters in *BLUE*—unrepresentative of actual Amundsen Sea conditions—it is equal to around 140 m.

In the ASP and the PIP the euphotic layer is generally shallower than 50 m and in places shallower than 40 m. This spatial pattern is due to the high concentrations of chlorophyll which are generated in the spring phytoplankton blooms close to DIS and pine island glacier (PIG).

The model simulations show a convection period starting in 2013 and continuing through 2014. We highlight this in Figure 1b, which shows a thick layer of CDW (temperature $> 0°C$) in Pine Island Bay (the sub-domain demarcated with a dashed line in Figure 1) from 2008 to 2012, which then collapses entirely during 2013. We emphasize the division between the realistic (2008–2012) and unrealistic (2013–2014) parts of the model run with the shading in Figure 2, and in all subsequent time series analyses.

In our model the spring bloom is initiated during October (Figure 2a), when the surface chlorophyll concentration averaged over Pine Island Bay first approaches 0.1 mg m^{-3}. Chlorophyll concentration then increases rapidly up to a peak on the order of 1 mg m^{-3}. The timing of this peak in November or December (depending on the year) is early relative to the observed peak in January (Arrigo et al., 2012). However the surface (0–10 m) chlorophyll concentration only represents one aspect of the bloom, with timing of the peak generally varying with depth (Twelves et al., 2020). In some years the initial spring bloom is followed by a distinct later bloom in February and March, likely the result of replenishment of nutrients due to wind-driven mixing (Castro de la Guardia
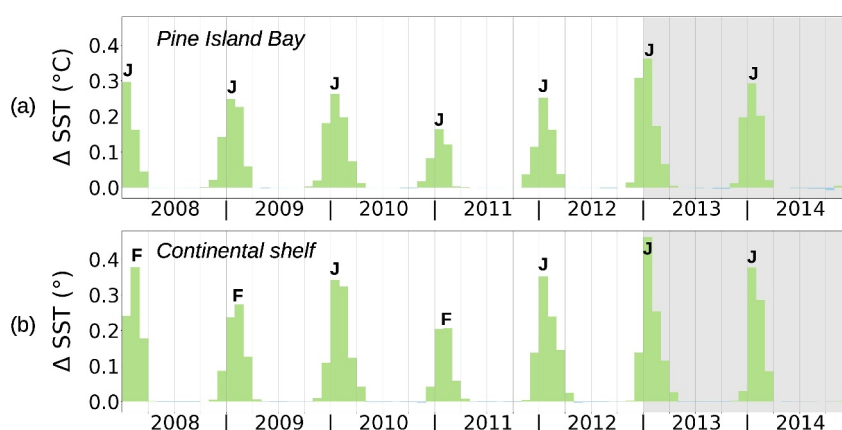
Figure 3. The anomaly in sea surface temperature due to chlorophyll, plotted for Pine Island Bay (a) and for the continental shelf as a whole (b). The month where the greatest anomaly occurs is marked in each case (J, January; F, February). Gray shading marks the period of convection.

et al., 2019). There is no clear trend in modeled chlorophyll production over the course of the study period, despite the onset of convection across parts of the domain.

The euphotic depth is largely insensitive to the interannual variability in surface chlorophyll concentration (Figure 2b). The minimum of around 40 m consistently occurs in December after a period of rapid shallowing, in line with the initiation of the spring bloom. The subsequent deepening of the euphotic depth is slower, generally remaining within 80 m of the surface until April.

A time series of satellite observations from the GlobColour database (http://hermes.acri.fr, black line in Figure 2b) shows that our model generally performs well in reproducing the magnitude of maximum and minimum euphotic depths. However there is a clear timing bias in the model, with the modeled minimum preceding the satellite data by around 1 month.

In situ observations have reported summertime euphotic depths in the polynya area of between 26 and 40 m (Park et al., 2017), which is shallow compared to our model range (Figure 1a; see also comparison in Figure S2 of Supporting Information S1). The strong response of shortwave attenuation to chlorophyll acts as a negative feedback on further phytoplankton growth (Manizza et al., 2008; Twelves et al., 2020), but here we focus instead on how it impacts physical processes within the Amundsen Sea.

3.2. SST Response to Chlorophyll

The average summertime SST across Pine Island Bay is elevated by between 0.2 °C and 0.3 °C in *GREEN* compared to *BLUE* (during the realistic period, Figure 3a), with the strongest anomalies occurring in January. A similar effect is apparent when averaging across the entire Amundsen Sea continental shelf (Figure 3b), though often peaking in February rather than January.

There is strong interannual variability in the magnitude of the anomaly, most visible in the relatively small size of the anomaly in January 2011 compared to the preceding and following years. The sensitivity to chlorophyll reaches almost 0.5 °C in January 2013, though this is during the start of the convection period.

Across the Amundsen Sea, the chlorophyll-driven surface warming is accompanied by a sub-surface cooling, such that the thermal stratification in most locations is strengthened (Figures S3 and S4 in Supporting Information S1). These changes, though relatively small, have the potential to impact access to both light and nutrients for phytoplankton (not shown).

3.3. Sea Ice Response to Chlorophyll

The open water area on the Amundsen Sea continental shelf (Figure 4a) shows similar interannual variability to the interannual variability in the sea surface temperature. In particular, the start of 2011 sees an unusually small
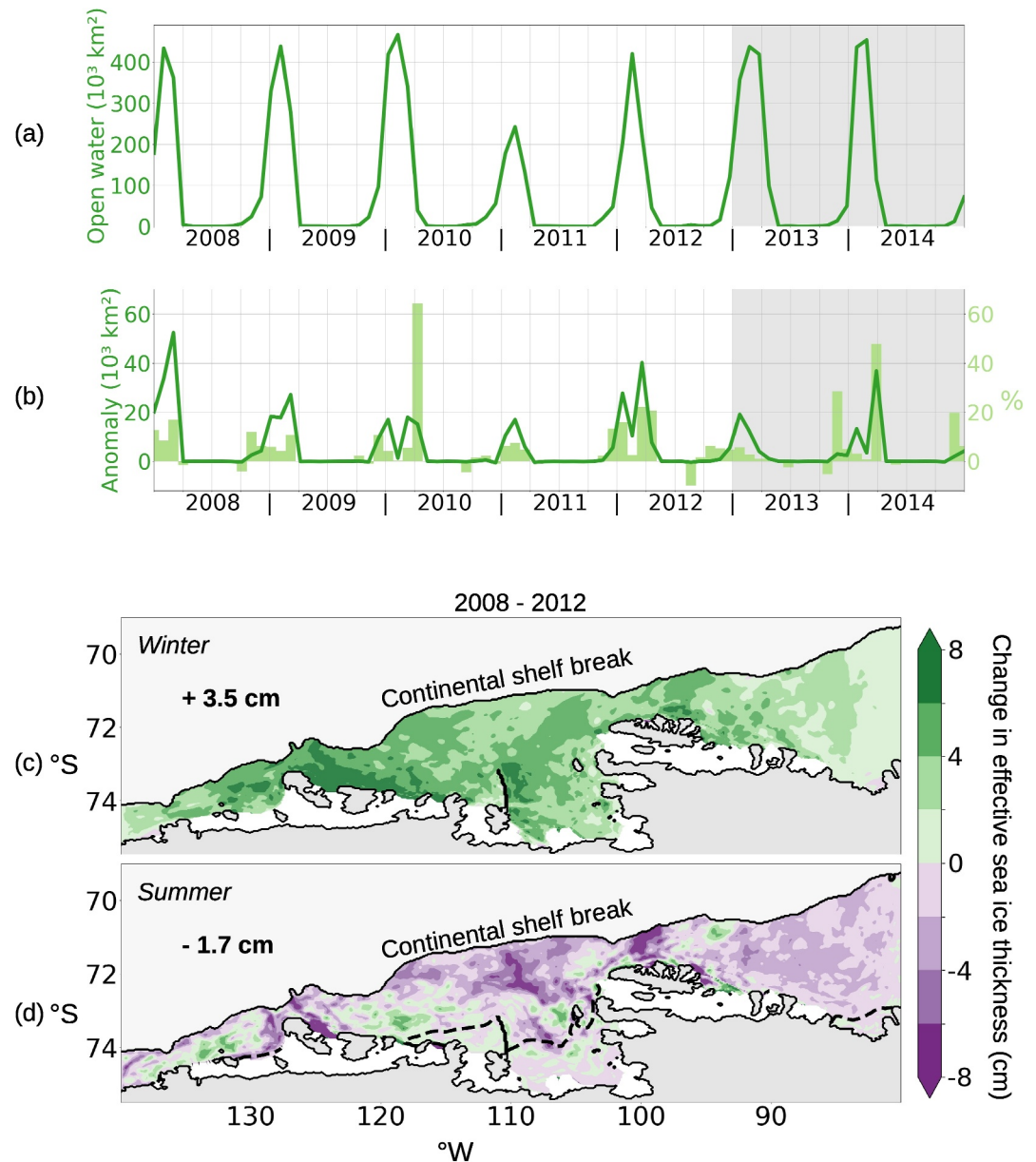
Figure 4. The total open water area on the Amundsen Sea continental shelf during the *GREEN* experiment (a), and the change in open water area compared to the *BLUE* experiment (b). In (b) the line shows the absolute change, whilst the bars show the relative percentage change in *GREEN* compared to *BLUE*. Relative changes are only plotted where the overall open water area exceeds 1,000 km^2. Also the impact of chlorophyll on wintertime (c) and summertime (d) effective sea ice thickness, that is, volume per unit area, averaging across months June to August in the former and across months December to February in the latter case. The position of the 10% sea ice cover threshold during summer is shown with the dashed line in (b). Also stated are the anomalies averaged across the continental shelf.

open water area at the same time as a relatively small SST anomaly between *BLUE* and *GREEN*. This suggests that chlorophyll may play a larger role in modifying heat fluxes in years when sea ice coverage is low.

With the addition of shortwave attenuation by chlorophyll in the *GREEN* experiment, the open water area expands by as much as 60% (in April 2010), and is consistently greater than in the *BLUE* experiment.

Sea ice volume, which we plot in Figures 4c and 4d using units of effective sea ice thickness (volume per unit ocean area), is also modified due to the presence of chlorophyll on the continental shelf. We investigate the

seasonality of this response by averaging over 2008–2012 separately for the winter (June–July–August) and summer (December–January–February) months.

In winter there is a net gain in sea ice volume in *GREEN* compared to *BLUE*, amounting to an increase in effective thickness of 3.5 cm (averaged across the shelf). The largest increases (exceeding 6 cm) are at the western edge of Pine Island Bay and along the front of Getz Ice Shelf.

In summer there is a net loss of sea ice volume due to chlorophyll, amounting to a decrease in effective thickness of 1.7 cm (averaged across the shelf). The largest decreases (exceeding 6 cm) are generally close to the continental shelf break. However there are also areas where the *GREEN* volume exceeds the *BLUE* volume even in summer, including close to the front of Getz Ice Shelf.

3.4. Surface Heat Balance

We consider each of the four components of the air-sea heat flux—shortwave radiation, longwave radiation, sensible heat transfer and latent heat transfer—only for those grid cells where sea ice coverage is below 10%. We choose this threshold—rather than the standard 15%—to reduce the residual contribution of ice to the overall surface heat flux (Figure S5 in Supporting Information S1). The response of each component to chlorophyll can be considered as the net effect of changes to the flux per unit area and changes to the total area A of open water available for heat exchange.

The patterns of sea ice extent—defined by the 10% threshold—show small differences between *GREEN* and *BLUE* (not shown), but to a large extent coincide. Thus the (ice-free) open water in the Amundsen Sea can be divided into a region that is common to both simulations, a region that is only ice-free in the *GREEN* model run, and a region that is only ice-free in the *BLUE* model run.

We start by considering only the *GREEN* heat fluxes in the common open water area (Figure 5a). Longwave radiation F_{LW} forms the largest component (approximate range 100–310 W m^{-2}) of the heat flux leaving open water, followed by latent heat (F_{LAT}, approximate range 40–160 W m^{-2}) and sensible heat (F_{SEN}, approximate range 0–80 W m^{-2}). Interannual variability is largest for sensible heat, and is smallest for latent heat.

The presence of chlorophyll in the *GREEN* experiment stimulates approximately 3–4 W m^{-2} of additional summertime sensible heat loss through the ice-free ocean surface, compared to *BLUE* (Figure 5b). This anomaly is substantial, around 20% of the overall sensible heat flux in *BLUE*. The latent heat flux anomaly is of similar absolute magnitude to the sensible heat flux anomaly (2–3 W m^{-2}), but of far smaller relative magnitude (less than 1% of the overall latent heat flux in *BLUE*) (Figure 5c). Finally, the additional longwave radiation (approximately 1–2 W m^{-2}) leaving the ice-free ocean surface in *GREEN* during summer is negligible relative to the magnitude of the overall longwave radiation flux (Figure 5d).

Next, we examine the combined impact of changes to heat flux in the common open water area and changes to heat flux resulting from the expansion of the open water area in *GREEN*. We switch from units of flux per unit area (W m^{-2}) to units of flux integrated over area (W) to quantify these two contributions to the anomaly.

In general, the sensible ($\mathbb{F}_{SEN}$, Figure 6a) and latent ($\mathbb{F}_{LAT}$, Figure 6b) heat flux anomalies are dominated by changes to heat flux through the common water area early in the season, and by changes in the marginal ice zone later in the season. More specifically, the slightly larger area of open water late in the summer in *GREEN* compared to *BLUE* allows for larger sensible and latent heat fluxes leaving the ocean. There is no such clear seasonal progression in the source of the longwave radiation anomaly ($\mathbb{F}_{LW}$, Figure 6c). Summed throughout the year (Figure 6d), sensible and latent heat flux anomalies are dominated by changes to heat flux in the common open water area, whereas the longwave radiation anomaly is dominated by an anomaly resulting from the changes to the open water area.

Though shortwave radiation per unit area incident on the sea surface is constant in the common polynya area, the integrated flux is higher in *GREEN* due to the increase in open water area (Figure 6e). The magnitude of the increase in shortwave radiation reaching the sea surface is around half of the total increase in heat loss from longwave, sensible and latent heat fluxes (Figure 6f).
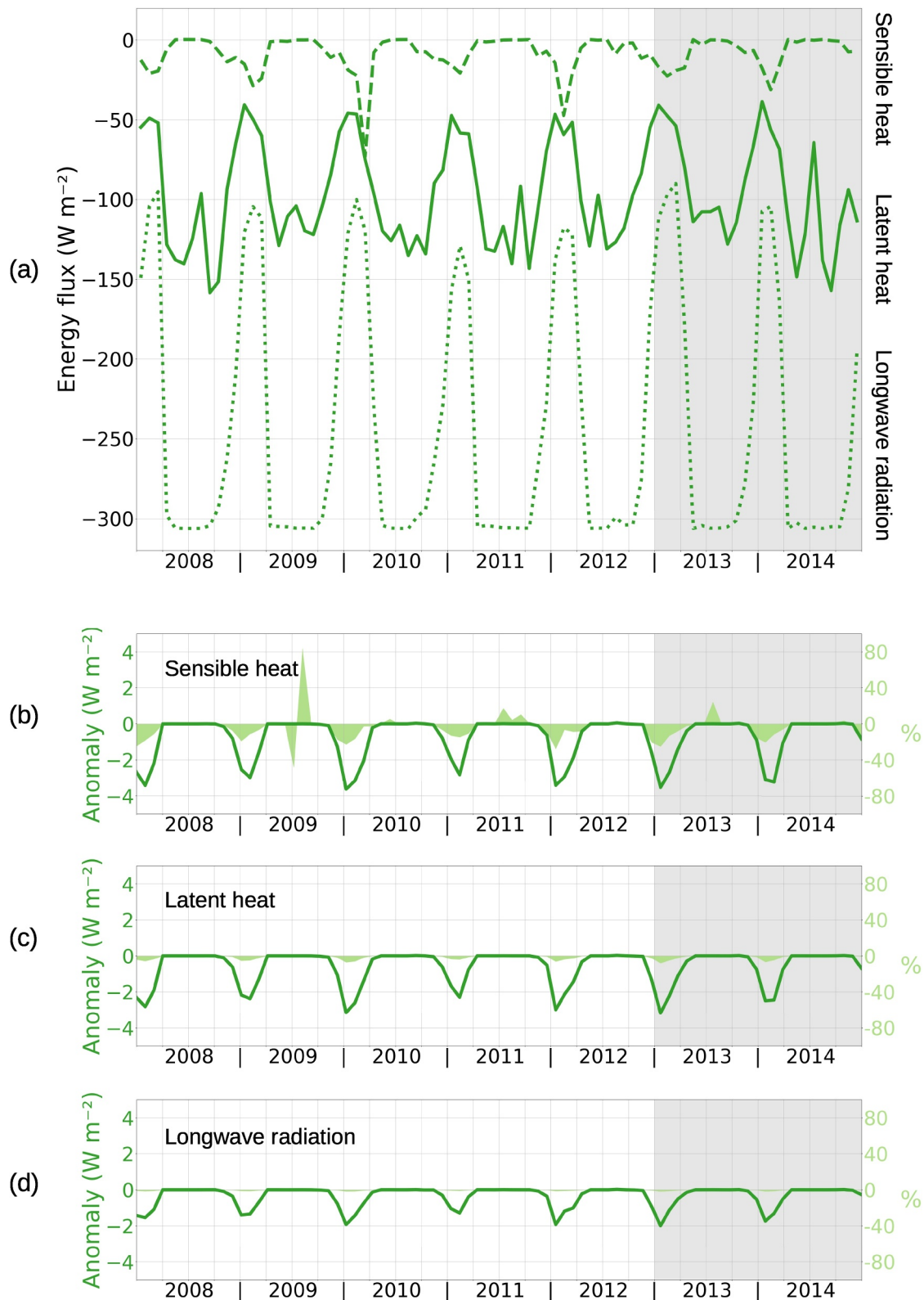
Figure 5. (a) Components of the heat flux per unit area from those areas of the Amundsen Sea which are ice-free in both *GREEN* and *BLUE*. Sensible heat, latent heat and longwave radiation are marked with dashed, solid and dotted lines respectively. Also (b–d) the magnitude of the heat flux anomaly per unit area for sensible, latent and longwave components respectively. Pale green shading shows the relative size of the anomaly, expressed as a percentage of the heat flux per unit area in *BLUE*.
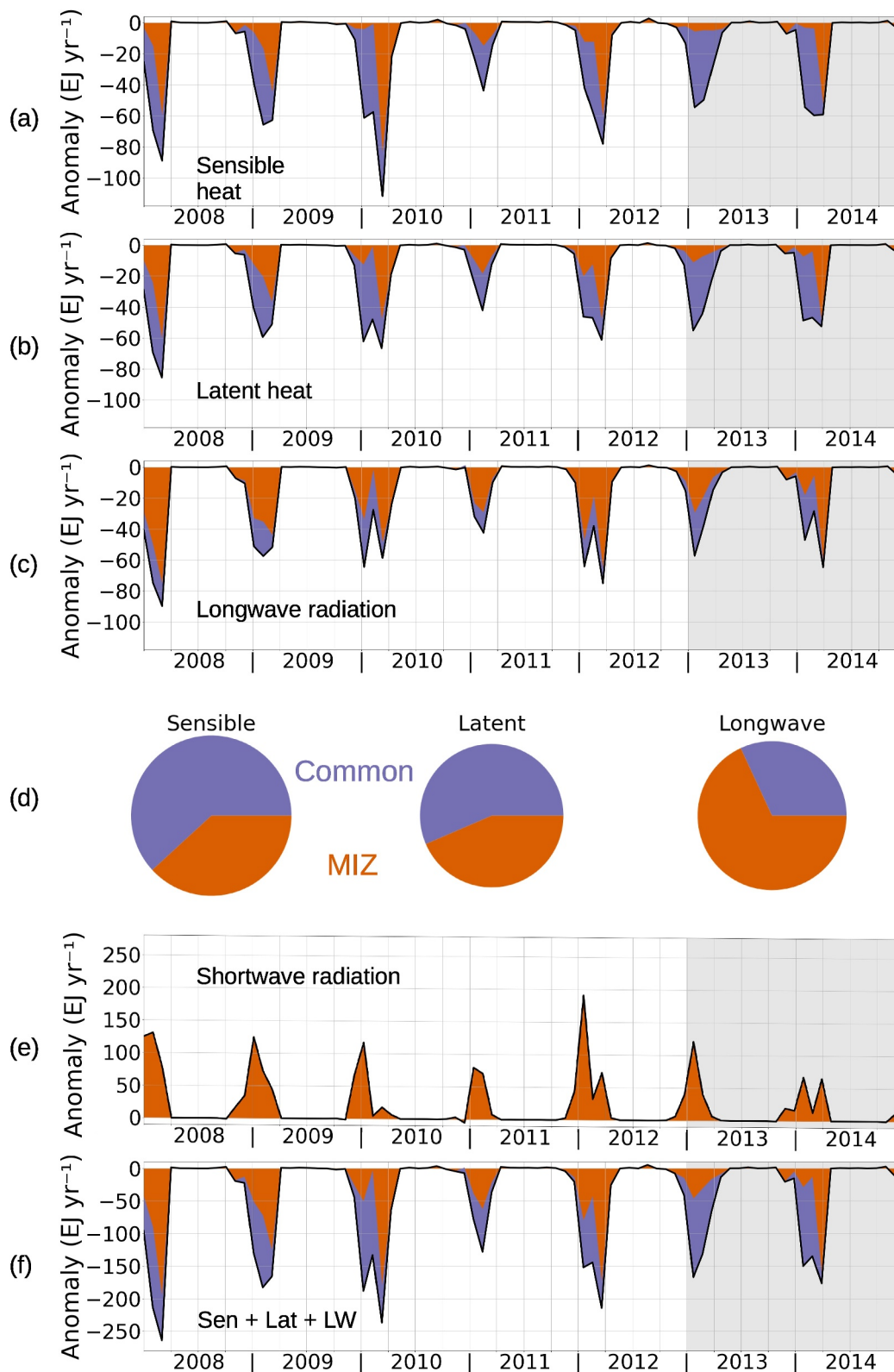
Figure 6. Magnitudes of the *GREEN - BLUE* heat flux anomaly for sensible (a), latent (b) and longwave (c) components, summing the changes within the common ice-free zone (purple shading) and changes to the extent of the ice-free zone (orange shading). The relative contributions of these two drivers summed across the time series are shown in (d). The positive anomaly in shortwave radiation resulting entirely from greater polynya area is shown in (e), and the total outgoing anomaly (summing components from (a–c)) is shown in (f).
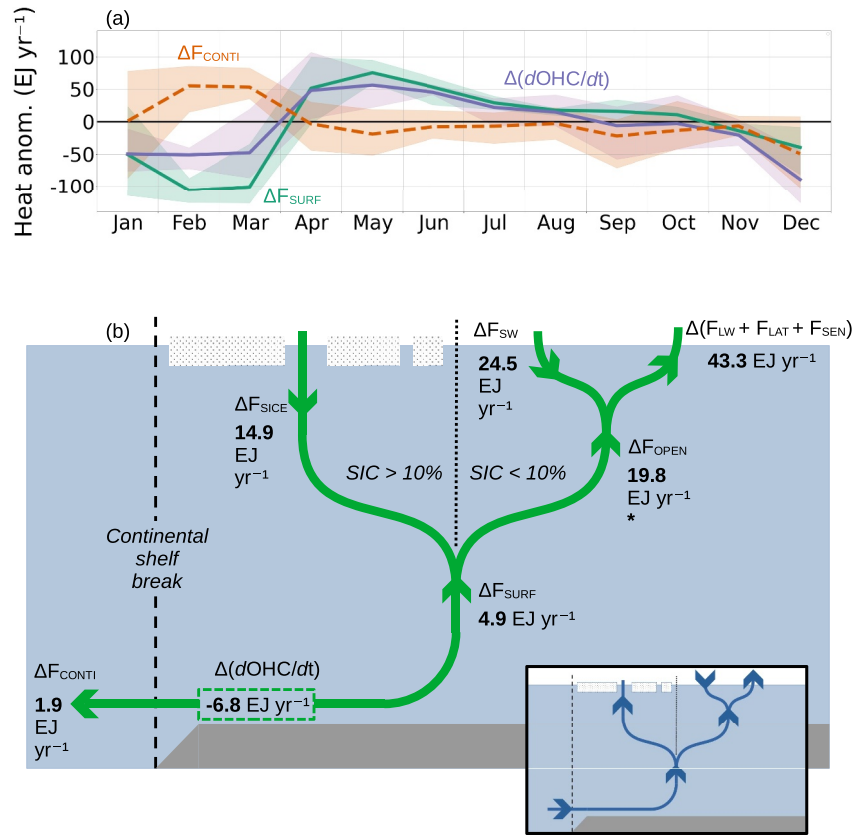
Figure 7. (a) Impact of chlorophyll on surface heat flux (green solid line), overall heat trend (purple line) and lateral heat transport calculated as a residual (orange dashed line), averaged across 2008–2012. Shading in the respective colors indicates the range in values over the 5 years. Also (b) a schematic of heat flux anomalies induced by chlorophyll, with values calculated by integrating model outputs from 2008 to 2012. The dashed line represents the location of the continental shelf break, whilst the dotted line represents the 10% sea ice edge. Green arrows represent the direction of flow of the energy *anomaly*—the direction of the energy flow itself is shown using the blue arrows on the inset figure. *The total surface energy flux from open water also includes a small residual term (Figure S5 in Supporting Information S1) which is not shown here.

3.5. Ocean Heat Content

Figure 7a shows the anomalies in ocean heat content, surface heat flux and lateral heat transport as a climatology over the years 2008–2012, thus avoiding the period of convection after 2012. The anomaly in the ocean heat trend $\frac{d}{dt}OHC$ on the continental shelf (defined as the region south of the 1,000 m isobath) evolves as

$$\Delta\left(\frac{d}{dt}OHC\right) = \Delta\mathbb{F}_{SURF} + \Delta\mathbb{F}_{CONTI} + \Delta\mathbb{F}_{CAV};$$ (13)

where $\Delta\mathbb{F}_{CONTI}$ is the anomaly in total lateral heat flux at the continental shelf break, $\Delta\mathbb{F}_{CAV}$ is the anomaly in total lateral heat flux at the front of ice shelf cavities, and $\Delta\mathbb{F}_{SURF}$ is the anomaly in surface heat flux. Then, assuming that $\Delta\mathbb{F}_{CAV} \ll \Delta\mathbb{F}_{CONTI}$, we estimate the anomaly in transport of heat onto the continental shelf as the residual

$$\Delta\mathbb{F}_{CONTI} \approx \Delta\left(\frac{d}{dt}OHC\right) - \Delta\mathbb{F}_{SURF}.$$ (14)

The net effect of increased shortwave radiation into the ocean and increased longwave, sensible and latent heat fluxes leaving the ocean is a loss of heat at the sea surface contained in the term $\Delta\mathbb{F}_{SURF}$. This chlorophyll-driven anomaly peaks at around 100 EJ yr^{-1} in February, but the surface heat loss is partially counteracted by a net gain in heat through transport of around 50 EJ yr^{-1}. During winter the anomaly in lateral heat transport is negligible.
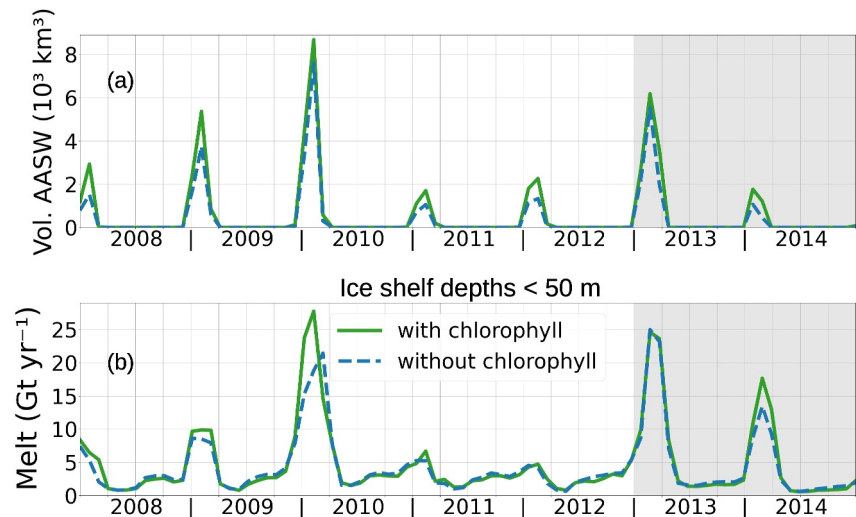
Figure 8. Time series showing the total volume of Antarctic Surface Water (AASW; defined by temperature > 0°C and salinity < 34.0 g kg^{-1}) on the continental shelf (a) and the total meltwater flux from the upper 50 m of ice shelves (b), for the *GREEN* and *BLUE* experiments.

However there is a substantial reduction in the wintertime heat lost to the atmosphere in *GREEN* relative to *BLUE*. Thus during winter $\Delta \mathbb{F}_{SURF}$ is positive, and this drives a positive (*GREEN* − *BLUE*) anomaly in the ocean heat trend, which peaks at just over 50 EJ yr^{-1} in May.

In Figure 7b we show a schematic representing the integration of these trends over the calendar year. The yearly changes are small compared to the seasonal changes shown in Figure 7a, but there is a robust signal of excess ocean cooling due to chlorophyll.

The impact of increased incoming shortwave and increased outgoing longwave, latent and sensible heat fluxes is an outgoing (*GREEN* − *BLUE*) anomaly of 19.8 EJ yr^{-1} from the open water portions of the Amundsen Sea continental shelf. In contrast, those areas covered by sea ice are subject to a net incoming anomaly of 14.9 EJ yr^{-1}. We do not attempt to diagnose the contributions to this latter anomaly, which is sensitive to the total open water area, to air-sea fluxes, and to fluxes between the sea ice and the ocean. Overall the presence of chlorophyll boosts Amundsen Sea surface heat loss by 4.9 EJ yr^{-1}. This is complemented by a net heat export anomaly of 1.9 EJ yr^{-1} leaving the continental shelf, producing an overall ocean cooling anomaly of 6.8 EJ yr^{-1} due to chlorophyll.

3.6. Impact on AASW and Near-Surface Melt Rates

The increased near-surface warming in the *GREEN* experiment drives changes to the AASW layer, defined here as the water mass lying on the continental shelf with temperature greater than 0 °C and salinity less than 34 g kg^{-1} (Figure 8a). In both experiments there is strong seasonality, but *GREEN* consistently shows a slightly greater volume of AASW.

The near-surface melt rate, defined here as the meltwater flux originating from shallower than 50 m on the ice shelf, shows strong interannual variability correlating with the volume of AASW. With more warm water close to the surface due to shortwave attenuation by chlorophyll, the shallowest portions of the ice shelves undergo stronger melting in *GREEN* compared to *BLUE* (Figure 8b). This strengthening is small in most years, but in early 2010 the peak near-surface melt rate is increased by over 20% due to chlorophyll.

3.7. Impact on CDW and Ice Shelf Melt Rates at Depth

Meanwhile the CDW layer, defined here as the water mass lying on the continental shelf with temperature greater than 0 °C and salinity greater than 34.5 g kg^{-1}, is relatively stable seasonally, but shows signs of the decadal variability seen in observations (Dutrieux et al., 2014), as well as the convection after 2012 reported by Naughten
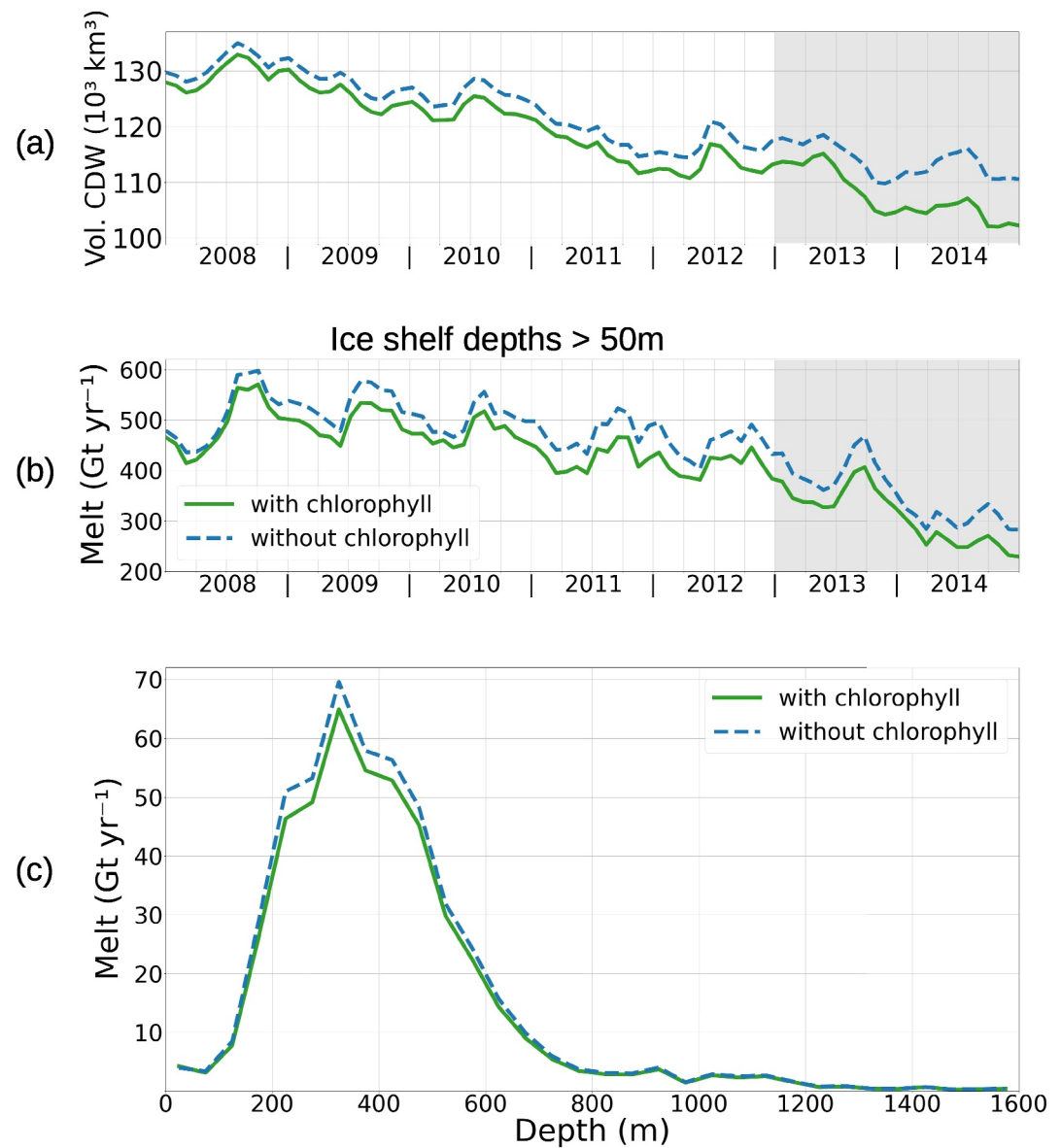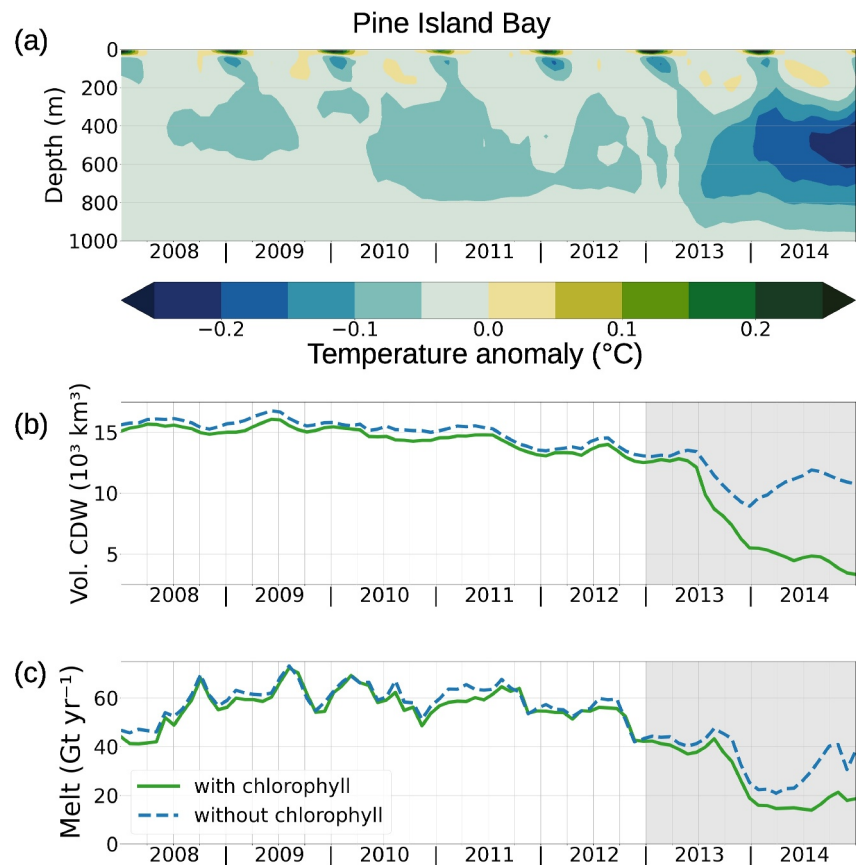
Figure 9. Time series showing the total volume of Circumpolar Deep Water (CDW; defined by temperature $> 0°C$ and salinity $> 34.5 \, \text{g kg}^{-1}$) on the continental shelf (a) and the total meltwater flux from below 50 m on the ice shelves (b), for the *GREEN* and *BLUE* experiments. Gray shading marks the period of convection. Also the ice shelf melt rate anomaly variation with respect to depth, shown here by binning over 50 m intervals (c).

et al. (2023). The volume of CDW is consistently less within *GREEN* compared to *BLUE*, but there is an increasing divergence between the time series over the study period (Figure 9a).

The time evolution of the total ice shelf meltwater flux (below 50 m) resembles that of the CDW volume, both in the trend and in the anomaly caused by chlorophyll (Figure 9b). The reduction in CDW on the continental shelf corresponds to a reduction in the heat ultimately available for basal melting. However whereas there is a clear divergence in the time series for CDW volume, the difference in melt rate remains on the order of 40 Gt yr^{-1} over the same period.

The majority of the anomaly between the two experiments comes from a chlorophyll-forced reduction in melt from ice lying between 200 and 500 m depth (Figure 9c). This is the same depth range where Naughten et al. (2023) report the greatest sensitivity of future Amundsen Sea melt rates to global emission scenarios.

Figure 10. Hovmöller diagram (a) showing the evolution of the Pine Island Bay temperature anomaly in *GREEN* with respect to the *BLUE* experiment, plus time series showing the total volume of circumpolar deep water in Pine Island Bay (b) and the total meltwater flux from ice shelves fringing Pine Island Bay (c). Gray shading marks the period of convection.

Integrating over all depths for the realistic period (2008–2012), the impact of chlorophyll is a reduction in melt rate of just under 7%, from 510 Gt yr^{-1} to 476 Gt yr^{-1}.

3.8. Impact of Chlorophyll During Model Convection Periods

The model undergoes periods of convection in both the *GREEN* and *BLUE* experiments, as it does with a Jerlov water-type scheme (Naughten et al., 2022). Figure 10 focuses on Pine Island Bay, where the onset of convection has a drastic effect on water mass structure (see also Figure 1b). While the convection may somewhat affect the model's applicability to the Amundsen Sea for this period, from the point of view of our process study it provides an opportunity to examine bio-optical feedbacks in a slightly different regime, one which may be applicable outside the region. We reiterate that this aspect of our analysis is not applicable to the actual conditions prevailing in the Amundsen region between 2008 and 2014.

Although the timing of the convection onset is the same for both experiments, the magnitude of the cooling is greater in *GREEN* than in *BLUE* (Figure 10a). Furthermore, the anomaly between the two experiments is substantially greater than that prior to the onset of convection at the end of 2012.

The convective cooling of the deepest waters translates into a decrease in the volume of CDW circulating around Pine Island Bay (Figure 10b). Again, the *GREEN—BLUE* anomaly during model convection is substantially greater than that during the realistic warm phase. Whereas in *BLUE* there remains a CDW volume of around 1.1 x 10^4 km in December 2014, in *GREEN* this is reduced to around 3,000 km.

In turn the ice shelves fringing Pine Island Bay, which respond only very weakly to chlorophyll before 2012, become highly sensitive to chlorophyll after 2012 (Figure 10c). During 2014 the total melt within the *GREEN*

experiment is approximately half that from the *BLUE* experiment. Whilst these results do not relate to expected conditions underneath PIG, they may be relevant to those parts of the Antarctic continental shelf outside the Amundsen Sea where CDW intrusions are weak.

4. Discussion

4.1. Sensitivity of Polynyas to Chlorophyll

In spring the retreat of sea ice in the Amundsen Sea and the re-emergence of polynyas leaves phytoplankton exposed to solar radiation. This causes phytoplankton to bloom and saturate the upper ocean with highly attenuating chlorophyll. Our setup of MITgcm simulates this sea ice retreat, whilst BLING reproduces the seasonal increases both in chlorophyll and in light attenuation. As more heat from the sun is trapped close to the surface there are changes to the polynya heat balance, which our changes to the MITgcm-BLING code allow us to evaluate.

The model skill in reproducing euphotic depth is a compound of the skill of the bio-optical model and the skill of the biogeochemical model. Modeled chlorophyll concentrations in Pine Island Bay of around 1 mg m^{-3} stimulate between 0.2°C and 0.3°C of additional surface warming on top of that which would result from attenuation by water molecules alone. Hence our results indicate that phytoplankton blooms could play a substantial role in determining the summertime sea surface temperature in polynyas. The anomaly is on the same order of magnitude as that reported when Manizza et al. (2005) originally implemented attenuation by chlorophyll in a global ocean model, and is in line with previous studies which showed that biologically mediated changes in SST could influence marine heatwaves and storm tracks (Gnanadesikan et al., 2010, 2019).

Attenuation by chlorophyll enhances the magnitude of the seasonal sea ice cycle, via thicker winter ice and thinner summertime ice, as originally observed in modeling on a global domain by Manizza et al. (2005). Ice effective thickness responds more weakly to chlorophyll in summer, whilst in winter it increases substantially. Though these changes are small overall relative to the interannual variability in sea ice cover, they represent a potential feedback mechanism, since it is the initial retreat of sea ice which itself stimulates, via biological production, the increase in near-surface heat attenuation.

Pefanis et al. (2020) found that light attenuation by CDOM caused a net summertime heat loss to the atmosphere across most of the Arctic in their model, but a net summertime heat gain close to the sea ice edge. They attribute the latter to reduced sea ice cover at the edge of the ice pack. We find that attenuation by chlorophyll generates similarly divergent effects in the Amundsen Sea, but within polynyas we are also able to separate the different terms contributing to this anomaly. Reduced ice coverage drives an increase in heat lost via longwave radiation. Increases in heat lost through sensible and latent heat fluxes are instead mostly driven by increased polynya SST. Overall, there is a net heat loss in open water areas (ice cover less than 10%) and a net heat gain in areas with ice cover greater than 10%.

As in previous modeling with BLING in the Amundsen Sea (Twelves et al., 2020), the simulated phytoplankton bloom is early relative to the observed bloom. In our case that means that by January the bloom is already in decline. Two effects of this bias could be imagined. On the one hand there is less chlorophyll to attenuate light when that attenuation would contribute most strongly to the heat budget. Conversely, the early bloom allows more time for the springtime surface warming to equilibrate with the atmosphere, which potentially exaggerates the impact of the SST anomaly on summertime heat loss to the atmosphere and minimizes the impact of the SST anomaly on sea ice.

Our work represents an initial attempt to quantify the impact of chlorophyll on polynya thermodynamics. In the future the values of the coefficients linking chlorophyll concentration to light attenuation should be constrained specifically for the mixture of diatoms and *P. antarctica* found in the Amundsen Sea (Lee et al., 2022), utilizing a combination of in situ and satellite observations. Ultimately, the use of a coupled ocean-atmosphere model would be necessary to accurately represent turbulent heat fluxes at the polynya surface, especially given the high sensitivity of sensible heat fluxes to small changes in the air-sea temperature gradient.

Recent years have seen dramatically lower sea ice extent in the Southern Ocean (Gilbert & Holmes, 2024; Purich & Doddridge, 2023). If this trend continues, then the sea surface in the region as a whole, including the continental shelf, will be exposed to substantially more shortwave radiation. Our study suggests that more attention should be

paid to the way that optically active constituents of the water column, particularly chlorophyll, attenuate this additional flux of shortwave radiation below the surface.

4.2. Sensitivity of Ice Shelves to Chlorophyll

In our study we consider only chlorophyll and thus exclude CDOM from our analysis. This can be justified based on the dominant role that chlorophyll plays in ocean color in the Southern Ocean overall (Dutkiewicz et al., 2015), but also based on the especially high chlorophyll concentrations that are driven by iron fluxes from ice shelves in the Amundsen Sea. However recent work by Son et al. (2023) found spatially variable CDOM concentrations in the Amundsen Sea, whilst particulate matter from ice shelves themselves may also contribute substantially to light attenuation (Murray et al., 2015).

Nonetheless our results indicate that chlorophyll plays a small but non-negligible role in modulating the quantity of warm and saline CDW present on the Amundsen Sea continental shelf. Over the simulation period, chlorophyll boosts heat loss to the atmosphere, cools the ocean, and leads to a decrease in the volume of CDW. With less warm and salty water at depth, basal melting is consistently—though weakly—reduced over the study period. We do not attempt in our study to diagnose the changes to lateral heat transport pathways, driven by changes to shortwave attenuation, that undoubtedly also influence the anomaly in basal melt rates.

Chlorophyll does not impact the shape of the melt rate distribution with respect to depth, and thus the greatest sensitivity is over the 200–500 m depth range where the bulk of basal melting occurs. This is also the same depth range where Naughten et al. (2023) showed that future melt rates are most sensitive to future emission scenario (their extended data Figure 8).

The overall melt rate trend in our results—and in the real Amundsen Sea—is driven by intrusions of modified Circumpolar Deep Water (CDW), which are in turn dominated by processes at the continental shelf break (Kimura et al., 2017). The years covered in our study form part of a period of decadal-scale cooling—with associated reductions in melt rate—on the Amundsen Sea continental shelf. On top of this trend, our model captures a small seasonal component relating to melting close to the sea surface. Here, within the upper 50 m of ice shelves, melt rates are driven by AASW and, since the AASW layer expands in response to chlorophyll, the net effect of chlorophyll is an increase in melt rates. This melting close to the front of ice shelves due to summertime heating of the surface ocean has been seen in some previous Amundsen Sea modeling (Twelves et al., 2020), but is little studied precisely because it is much smaller in magnitude than the basal melting that occurs at depth.

Jacobs et al. (1992) introduced the partition of ice shelf melting between three distinct modes. Mode I melting occurs when dense shelf water, mixed downward from the surface, is pushed to a depth where its temperature exceeds the in situ melting point. Mode II melting occurs when already warm and saline CDW moves onto the continental shelf and floods ice shelf cavities, whilst Mode III melting occurs when the ocean surface is warmed seasonally and then moves beneath the ice shelf front. Using this terminology, the Amundsen Sea is heavily dominated by Mode II melting, with a much smaller contribution from Mode III. Mode I melting does not currently occur on the Amundsen Sea shelf, though it may have in the past, and may occur in our model during convection periods. We see in our results that when convection does occur, the impact of chlorophyll on melt rates is far greater, and so we suggest similar studies should be conducted in those locations, such as the Weddell Sea, where Mode I melting is thought to take place.

Stewart et al. (2019) showed that melting beneath the frontal zone of Ross Ice Shelf is to a large extent driven by solar radiation absorbed in the adjacent polynya. This Mode III melting occurs adjacent to a relatively large phytoplankton bloom affecting ocean color (Arrigo & Van Dijken, 2003). Based on our results, we expect that this bloom modulates AASW content in the Ross Sea polynya and thus affects the transfer of solar heating to the ice shelf. The expanded coverage of biogeochemical Argo floats to the Ross Sea continental shelf [under the SOCCOM program, Sarmiento et al., 2023] will provide physical and biogeochemical data sets that could complement future modeling in this direction. Meanwhile in East Antarctica Herraiz-Borreguero et al. (2016), have shown that Mode III melting can drive large iron fluxes from the Amery Ice Shelf to Prydz Bay. This raises the prospect of complex interactions between phytoplankton blooms and iron supply in some locations; whereby an ice shelf provides part of the iron supply to a phytoplankton bloom, but the bloom itself affects the flux of iron leaving the ice shelf cavity.

5. Conclusion

In this study we have demonstrated that the same phytoplankton blooms that rely on nearby ice shelves for supply of nutrients (most especially iron) can themselves affect the supply of oceanic heat that drives basal melting. The production of chlorophyll in the spring bloom strengthens the attenuation of shortwave radiation in the visible wavelengths, so that more solar energy is dissipated close to the polynya surface. Here this heat is more easily lost to the atmosphere in longwave, sensible and latent heat fluxes. Meanwhile the reduced solar radiation below the surface layers leaves deeper waters cooler than they would be in the absence of phytoplankton. As this cooler layer interacts with CDW below, the bio-optical feedback ultimately reduces melting from Amundsen Sea ice shelves by between 2% and 13% (varying over the study period). On average, melt rates are approximately 7% lower than would be the case in the complete absence of chlorophyll.

Here we examine the thermodynamic impact of chlorophyll only in the Amundsen Sea, a region characterized by latent heat-dominated polynyas and Mode II-dominated ice shelves. However by extending our analysis to years where the model shows convection not seen in observations, we infer that chlorophyll likely has a stronger impact on ice shelf melting at those locations where Mode II does not dominate. Similarly, whilst our model results show moderate impacts of chlorophyll on SST and sea ice in latent heat polynyas, it is likely that biologically productive sensible heat polynyas—formed by the upwelling of warmer water from depth (Prend et al., 2019)—would be more sensitive to chlorophyll, given their purely thermodynamic origin. At present, it is challenging to investigate the bio-optical feedback with observations, and thus further numerical modeling is merited to investigate this mechanism both in the Amundsen Sea and on the broader Southern Ocean scale.

Acronyms

DIS	Dotson Ice Shelf
PIIS	Pine Island Ice Shelf
PIP	Pine Island Polynya
ASP	Amundsen Sea Polynya
PIB	Pine Island Bay
NPP	Net Primary Production
NCP	Net Community Production
CDW	Circumpolar Deep Water
WW	Winter Water
AASW	Antarctic Surface Water
BLING	Biology Light Iron Nutrients Gases model
B-SOSE	Biogeochemical Southern Ocean State Estimation
MITgcm	Massachusetts Institute of Technology general circulation model
KPP	K-Profile Parameterization of vertical mixing.

Data Availability Statement

MITgcm code can be accessed publicly at mitgcm.org and the MITgcm manual is available for the latest checkpoint (Campin et al., 2023). B-SOSE outputs are available at http://sose.ucsd.edu/bsose_solution_Iter105.html. The modified code coupling biology and physics is available at https://github.com/atwelves/MITgcm/tree/master; model inputs are available at an open-access repository (Twelves et al., 2024a), as are the model outputs used to plot figures in this manuscript (Twelves et al., 2024b). Scripts used to produce figures are filed under the release https://github.com/atwelves/Chlorophyll-production-in-the-Amundsen-Sea/releases/tag/publication. GlobColour data (http://globcolour.info) used in this study has been developed, validated, and distributed by ACRI-ST, France.

References

Alderkamp, A.-C., Mills, M. M., van Dijken, G. L., Laan, P., Thuróczy, C.-E., Gerringa, L. J., et al. (2012). Iron from melting glaciers fuels phytoplankton blooms in the Amundsen Sea (Southern ocean): Phytoplankton characteristics and productivity. *Deep Sea Research Part II: Topical Studies in Oceanography*, *71*, 32–48. https://doi.org/10.1016/j.dsr2.2012.03.005

Arneborg, L., Wåhlin, A., Björk, G., Liljebladh, B., & Orsi, A. (2012). Persistent inflow of warm water onto the central Amundsen shelf. *Nature Geoscience*, *5*(12), 876–880. https://doi.org/10.1038/ngeo1644

Arrigo, K. R., Lowry, K. E., & van Dijken, G. L. (2012). Annual changes in sea ice and phytoplankton in polynyas of the Amundsen sea, Antarctica. *Deep Sea Research Part II: Topical Studies in Oceanography*, *71*, 5–15.

Arrigo, K. R., & Van Dijken, G. L. (2003). Phytoplankton dynamics within 37 Antarctic coastal polynya systems. *Journal of Geophysical Research*, *108*(C8), 3271. https://doi.org/10.1029/2002jc001739

Arrigo, K. R., van Dijken, G. L., & Strong, A. L. (2015). Environmental controls of marine productivity hot spots around Antarctica. *Journal of Geophysical Research: Oceans*, *120*(8), 5545–5565. https://doi.org/10.1002/2015JC010888

Assmann, K., Jenkins, A., Shoosmith, D., Walker, D., Jacobs, S., & Nicholls, K. (2013). Variability of circumpolar deep water transport onto the Amundsen sea continental shelf through a shelf break trough. *Journal of Geophysical Research: Oceans*, *118*(12), 6603–6620. https://doi.org/10.1002/2013jc008871

Bett, D. T., Holland, P. R., Naveira Garabato, A. C., Jenkins, A., Dutrieux, P., Kimura, S., & Fleming, A. (2020). The impact of the Amundsen sea freshwater balance on ocean melting of the West Antarctic ice sheet. *Journal of Geophysical Research: Oceans*, *125*(9), e2020JC016305. https://doi.org/10.1029/2020jc016305

Bryan, F., Kauffman, B., Large, W., & Gent, P. (1996). Ncar csm flux coupler. Technical note (Tech. Rep.). *National Centre for Atmospheric Research*.

Cahill, B. E., Kowalczuk, P., Kritten, L., Gräwe, U., Wilkin, J., & Fischer, J. (2023). Estimating the seasonal impact of optically significant water constituents on surface heating rates in the Western Baltic Sea. *Biogeosciences*, *20*(13), 2743–2768. https://doi.org/10.5194/bg-20-2743-2023

Campin, J.-M., Heimbach, P., Losch, M., Forget, G., Amolod, D., Menemenlis, D., et al. (2023). Mitgcm/mitgcm: Ckeckpoint68r (version checkpoint68r) [Software]. *Zenodo*. https://doi.org/10.5281/zenodo.1409237

Castro de la Guardia, L., Garcia-Quintana, Y., Claret, M., Hu, X., Galbraith, E., & Myers, P. G. (2019). Assessing the role of high-frequency winds and sea ice loss on arctic phytoplankton blooms in an ice-ocean-biogeochemical model. *Journal of Geophysical Research: Biogeosciences*, *124*(9), 2728–2750. https://doi.org/10.1029/2018jg004869

Christie, F. D., Bingham, R. G., Gourmelen, N., Tett, S. F., & Muto, A. (2016). Four-decade record of pervasive grounding line retreat along the Bellingshausen margin of west Antarctica. *Geophysical Research Letters*, *43*(11), 5741–5749. https://doi.org/10.1002/2016gl068972

Dierssen, H. M., & Smith, R. C. (2000). Bio-optical properties and remote sensing ocean Color algorithms for Antarctic Peninsula waters. *Journal of Geophysical Research*, *105*(C11), 26301–26312. https://doi.org/10.1029/1999jc000296

Dinniman, M. S., St-Laurent, P., Arrigo, K. R., Hofmann, E. E., & van Dijken, G. L. (2020). Analysis of iron sources in Antarctic continental shelf waters. *Journal of Geophysical Research: Oceans*, *125*(5), e2019JC015736. https://doi.org/10.1029/2019jc015736

Dutkiewicz, S., Hickman, A., Jahn, O., Gregg, W., Mouw, C., & Follows, M. (2015). Capturing optically important constituents and properties in a marine biogeochemical and ecosystem model. *Biogeosciences*, *12*(14), 4447–4481. https://doi.org/10.5194/bg-12-4447-2015

Dutrieux, P., De Rydt, J., Jenkins, A., Holland, P. R., Ha, H. K., Lee, S. H., et al. (2014). Strong sensitivity of pine island ice-shelf melting to climatic variability. *Science*, *343*(6167), 174–178. https://doi.org/10.1126/science.1244341

Galbraith, E. D., Gnanadesikan, A., Dunne, J. P., & Hiscock, M. R. (2010). Regional impacts of iron-light Colimitation in a global biogeochemical model. *Biogeosciences*, *7*(3), 1043–1064. https://doi.org/10.5194/bg-7-1043-2010

Gerringa, L. J., Alderkamp, A.-C., Laan, P., Thuroczy, C.-E., De Baar, H. J., Mills, M. M., et al. (2012). Iron from melting glaciers fuels the phytoplankton blooms in Amundsen Sea (Southern ocean): Iron biogeochemistry. *Deep Sea Research Part II: Topical Studies in Oceanography*, *71*, 16–31. https://doi.org/10.1016/j.dsr2.2012.03.007

Gilbert, E., & Holmes, C. (2024). 2023's Antarctic sea ice extent is the lowest on record. *Weather*, *79*(2), 46–51. https://doi.org/10.1002/wea.4518

Gnanadesikan, A., Emanuel, K., Vecchi, G. A., Anderson, W. G., & Hallberg, R. (2010). How ocean color can steer Pacific tropical cyclones. *Geophysical Research Letters*, *37*(18), L18802. https://doi.org/10.1029/2010gl044514

Gnanadesikan, A., Kim, G. E., & Pradal, M.-A. S. (2019). Impact of colored dissolved materials on the annual cycle of sea surface temperature: Potential implications for extreme ocean temperatures. *Geophysical Research Letters*, *46*(2), 861–869. https://doi.org/10.1029/2018gl080695

Goldberg, D. N., Twelves, A. G., Holland, P. R., & Wearing, M. G. (2023). The non-local impacts of Antarctic subglacial runoff. *Journal of Geophysical Research: Oceans*, *128*(10), e2023JC019823. https://doi.org/10.1029/2023jc019823

Gourmelen, N., Goldberg, D. N., Snow, K., Henley, S. F., Bingham, R. G., Kimura, S., et al. (2017). Channelized melting drives thinning under a rapidly melting Antarctic ice shelf. *Geophysical Research Letters*, *44*(19), 9796–9804. https://doi.org/10.1002/2017gl074929

Hernandez, O., Jouanno, J., Echevin, V., & Aumont, O. (2017). Modification of sea surface temperature by chlorophyll concentration in the Atlantic upwelling systems. *Journal of Geophysical Research: Oceans*, *122*(7), 5367–5389. https://doi.org/10.1002/2016jc012330

Herraiz-Borreguero, L., Lannuzel, D., Van Der Merwe, P., Treverrow, A., & Pedro, J. (2016). Large flux of iron from the Amery ice shelf marine ice to Prydz bay, East Antarctica. *Journal of Geophysical Research: Oceans*, *121*(8), 6009–6020. https://doi.org/10.1002/2016jc011687

Hersbach, H., Bell, B., Berrisford, P., Hirahara, S., Horányi, A., Muñoz-Sabater, J., et al. (2020). The ERA5 global reanalysis. *Quarterly Journal of the Royal Meteorological Society*, *146*(730), 1999–2049. https://doi.org/10.1002/qj.3803

Jacobs, S., Helmer, H., Doake, C., Jenkins, A., & Frolich, R. (1992). Melting of ice shelves and the mass balance of Antarctica. *Journal of Glaciology*, *38*(130), 375–387. https://doi.org/10.1017/s0022143000002252

Jerlov, N. G. (1976). *Marine optics*. Elsevier.

Kimura, S., Jenkins, A., Regan, H., Holland, P. R., Assmann, K. M., Whitt, D. B., et al. (2017). Oceanographic controls on the variability of ice-shelf basal melting and circulation of glacial meltwater in the Amundsen Sea embayment, Antarctica. *Journal of Geophysical Research: Oceans*, *122*(12), 10131–10155. https://doi.org/10.1002/2017jc012926

Large, W. G., McWilliams, J. C., & Doney, S. C. (1994). Oceanic vertical mixing: A review and a model with a nonlocal boundary layer parameterization. *Reviews of Geophysics*, *32*(4), 363–403. https://doi.org/10.1029/94rg01872

Lee, Y., Park, J., Jung, J., & Kim, T. W. (2022). Unprecedented differences in phytoplankton community structures in the Amundsen Sea polynyas, West Antarctica. *Environmental Research Letters*, *17*(11), 114022. https://doi.org/10.1088/1748-9326/ac9a5f

Locarnini, M., Mishonov, A., Baranova, O., Boyer, T., Zweng, M., Garcia, H., et al. (2018). World ocean atlas 2018, volume 1: Temperature.

Losch, M. (2008). Modeling ice shelf cavities in AZ coordinate ocean general circulation model. *Journal of Geophysical Research*, *113*(C8), C08043. https://doi.org/10.1029/2007jc004368

Losch, M., Menemenlis, D., Campin, J.-M., Heimbach, P., & Hill, C. (2010). On the formulation of sea-ice models. Part 1: Effects of different solver implementations and parameterizations. *Ocean Modelling*, *33*(1–2), 129–144. https://doi.org/10.1016/j.ocemod.2009.12.008

Manizza, M., Le Quéré, C., Watson, A. J., & Buitenhuis, E. T. (2005). Bio-optical feedbacks among phytoplankton, upper ocean physics and sea-ice in a global model. *Geophysical Research Letters*, *32*(5), L05603. https://doi.org/10.1029/2004gl020778

Manizza, M., Le Quéré, C., Watson, A. J., & Buitenhuis, E. T. (2008). Ocean biogeochemical response to phytoplankton-light feedback in a global model. *Journal of Geophysical Research*, *113*(C10), C10010. https://doi.org/10.1029/2007jc004478

Marshall, J., Hill, C., Perelman, L., & Adcroft, A. (1997). Hydrostatic, quasi-hydrostatic, and nonhydrostatic ocean modeling. *Journal of Geophysical Research*, *102*(C3), 5733–5752. https://doi.org/10.1029/96jc02776

Morel, A. (1988). Optical modeling of the upper ocean in relation to its biogenous matter content (case I waters). *Journal of Geophysical Research*, *93*(C9), 10749–10768. https://doi.org/10.1029/jc093ic09p10749

Morlighem, M., Rignot, E., Binder, T., Blankenship, D., Drews, R., Eagles, G., et al. (2020). Deep glacial troughs and stabilizing ridges unveiled beneath the margins of the Antarctic ice sheet. *Nature Geoscience*, *13*(2), 132–137. https://doi.org/10.1038/s41561-019-0510-8

Murray, C., Markager, S., Stedmon, C. A., Juul-Pedersen, T., Sejr, M. K., & Bruhn, A. (2015). The influence of glacial melt water on bio-optical properties in two contrasting Greenlandic fjords. *Estuarine, Coastal and Shelf Science*, *163*, 72–83. https://doi.org/10.1016/j.ecss.2015.05.041

Naughten, K. A., Holland, P. R., & De Rydt, J. (2023). Unavoidable future increase in west Antarctic ice-shelf melting over the twenty-first century. *Nature Climate Change*, *13*(11), 1222–1228. https://doi.org/10.1038/s41558-023-01818-x

Naughten, K. A., Holland, P. R., Dutrieux, P., Kimura, S., Bett, D. T., & Jenkins, A. (2022). Simulated twentieth-century ocean warming in the Amundsen Sea, West Antarctica. *Geophysical Research Letters*, *49*(5), e2021GL094566. https://doi.org/10.1029/2021gl094566

Nissen, C., & Vogt, M. (2021). Factors controlling the competition between *Phaeocystis* and diatoms in the southern ocean and implications for carbon export fluxes. *Biogeosciences*, *18*(1), 251–283. https://doi.org/10.5194/bg-18-251-2021

Oliver, H., St-Laurent, P., Sherrell, R. M., & Yager, P. L. (2019). Modeling iron and light controls on the summer Phaeocystis Antarctica bloom in the Amundsen Sea polynya. *Global Biogeochemical Cycles*, *33*(5), 570–596. https://doi.org/10.1029/2018GB006168

Park, J., Kuzminov, F. I., Bailleul, B., Yang, E. J., Lee, S., Falkowski, P. G., & Gorbunov, M. Y. (2017). Light availability rather than Fe controls the magnitude of massive phytoplankton bloom in the Amundsen Sea polynyas, Antarctica. *Limnology & Oceanography*, *62*(5), 2260–2276. https://doi.org/10.1002/lno.10565

Pefanis, V., Losa, S. N., Losch, M., Janout, M. A., & Bracher, A. (2020). Amplified arctic surface warming and sea ice loss due to phytoplankton and colored dissolved material. *Geophysical Research Letters*, *47*(21), e2020GL088795. https://doi.org/10.1029/2020gl088795

Prend, C. J., Gille, S. T., Talley, L. D., Mitchell, B. G., Rosso, I., & Mazloff, M. R. (2019). Physical drivers of phytoplankton bloom initiation in the southern ocean's scotia sea. *Journal of Geophysical Research: Oceans*, *124*(8), 5811–5826. https://doi.org/10.1029/2019jc015162

Purich, A., & Doddridge, E. W. (2023). Record low Antarctic sea ice coverage indicates a new sea ice state. *Communications Earth & Environment*, *4*(1), 314. https://doi.org/10.1038/s43247-023-00961-9

Sarmiento, J. L., Johnson, K. S., Arteaga, L. A., Bushinsky, S. M., Cullen, H. M., Gray, A. R., et al. (2023). The Southern Ocean carbon and climate observations and modeling (soccom) project: A review. *Progress in Oceanography*, *219*, 103130. https://doi.org/10.1016/j.pocean.2023.103130

Shean, D. E., Joughin, I. R., Dutrieux, P., Smith, B. E., & Berthier, E. (2019). Ice shelf basal melt rates from a high-resolution Digital Elevation Model (DEM) record for pine island glacier, Antarctica. *The Cryosphere*, *13*(10), 2633–2656. https://doi.org/10.5194/tc-13-2633-2019

Shepherd, A., Gilbert, L., Muir, A. S., Konrad, H., McMillan, M., Slater, T., et al. (2019). Trends in Antarctic ice sheet elevation and mass. *Geophysical Research Letters*, *46*(14), 8174–8183. https://doi.org/10.1029/2019gl082182

Son, J., Jung, J., Lee, Y., Kim, T.-W., Park, J., Jeon, M. H., & Park, M. O. (2023). Contrasting optical properties of dissolved organic matter between oceanic regions near the Getz and Dotson ice shelves in the Amundsen Sea, West Antarctica. *Marine Chemistry*, *258*, 104335. https://doi.org/10.1016/j.marchem.2023.104335

Stewart, C. L., Christoffersen, P., Nicholls, K. W., Williams, M. J., & Dowdeswell, J. A. (2019). Basal melting of ross ice shelf from solar heat absorption in an ice-front polynya. *Nature Geoscience*, *12*(6), 435–440. https://doi.org/10.1038/s41561-019-0356-0

St-Laurent, P., Klinck, J., & Dinniman, M. (2015). Impact of local winter cooling on the melt of pine island glacier, Antarctica. *Journal of Geophysical Research: Oceans*, *120*(10), 6718–6732. https://doi.org/10.1002/2015jc010709

St-Laurent, P., Yager, P. L., Sherrell, R. M., Oliver, H., Dinniman, M. S., & Stammerjohn, S. E. (2019). Modelling the seasonal cycle of iron and carbon fluxes in the Amundsen Sea polynya, Antarctica. *Journal of Geophysical Research: Oceans*, *124*(3), 1544–1565. https://doi.org/10.1029/2018JC014773

St-Laurent, P., Yager, P. L., Sherrell, R. M., Stammerjohn, S. E., & Dinniman, M. S. (2017). Pathways and supply of dissolved iron in the Amundsen Sea (Antarctica). *Journal of Geophysical Research: Oceans*, *122*(9), 7135–7162. https://doi.org/10.1002/2017JC013162

Tamsitt, V., Talley, L. D., Mazloff, M. R., & Cerovečki, I. (2016). Zonal variations in the Southern Ocean heat budget. *Journal of Climate*, *29*(18), 6563–6579. https://doi.org/10.1175/jcli-d-15-0630.1

Twelves, A. G., Goldberg, D. N., Henley, S. F., Mazloff, M., & Jones, D. (2020). Self-shading and meltwater spreading control the transition from light to iron limitation in an Antarctic coastal polynya. *Journal of Geophysical Research: Oceans*, *126*(2), e2020JC016636. https://doi.org/10.1029/2020jc016636

Twelves, A. G., Goldberg, D. N., Holland, P. R., Henley, S. F., Mazloff, M. R., & Jones, D. C. (2024a). Chlorophyll production in the amundsen sea boosts heat flux to atmosphere and weakens heat flux to ice shelves - Model inputs [Dataset]. *Zenodo*. https://doi.org/10.5281/zenodo.12731891

Twelves, A. G., Goldberg, D. N., Holland, P. R., Henley, S. F., Mazloff, M. R., & Jones, D. C. (2024b). Chlorophyll production in the Amundsen Sea boosts heat flux to atmosphere and weakens heat flux to ice shelves—Model outputs [Dataset]. *Zenodo*. https://doi.org/10.5281/zenodo.10830064

Verdy, A., & Mazloff, M. R. (2017). A data assimilating model for estimating southern ocean biogeochemistry. *Journal of Geophysical Research: Oceans*, *122*(9), 6968–6988. https://doi.org/10.1002/2016JC012650

Yager, P. L., Sherrell, R., Sipler, R., Ducklow, H., Schofield, O., Ingall, E., et al. (2016). A carbon budget for the Amundsen Sea polynya, Antarctica: Estimating net community production and export in a highly productive polar ecosystem. *Elementa-Science Of The Anthropocene*, *4*(140), 000140. https://doi.org/10.12952/journal.elementa.000140

Yu, X., Lee, Z., Shang, S., Wang, M., & Jiang, L. (2022). Estimating the water-leaving albedo from ocean color. *Remote Sensing of Environment*, *269*, 112807. https://doi.org/10.1016/j.rse.2021.112807

Zheng, Y., Heywood, K. J., Webber, B. G., Stevens, D. P., Biddle, L. C., Boehme, L., & Loose, B. (2021). Winter seal-based observations reveal glacial meltwater surfacing in the Southeastern Amundsen Sea. *Communications Earth & Environment*, *2*(1), 1–9. https://doi.org/10.1038/s43247-021-00111-z

Zweng, M., Seidov, D., Boyer, T., Locarnini, M., Garcia, H., Mishonov, A., et al. (2019). World ocean atlas 2018, volume 2: Salinity.